Acknowledgement

This paper is published by ASCE
Journal of Structural Engineering, 2022, Vol 148, issue 12

https://doi.org/10.1061/JSENDH.STENG-10688

AN ADAPTIVE FIBER SECTION DISCRETIZATION SCHEME FOR NONLINEAR FRAME ANALYSIS

Svetlana M. Kostic[1] and Filip C. Filippou[2]

[1]Ph.D., University of Belgrade Faculty of Civil Engineering, Bulevar kralja Aleksandra 73, 11000 Belgrade, Serbia. Email: svetlana@grf.bg.ac.rs (corresponding author)

[2]Professor, Department of Civil and Environmental Engineering, University of California, Berkeley, CA 94720-1710. Email: filippou@berkeley.edu

ABSTRACT

The paper proposes an adaptive fiber section discretization scheme for inelastic frame elements. The scheme uses cubature rules for the efficient and accurate evaluation of the section response over the elastic portion of the section. As inelastic strains arise and penetrate into the section from the edges, the scheme converts the area under inelastic strains to a regular fiber discretization. This approach offers considerable advantages for the computational efficiency of large structural models with inelastic frame elements by minimizing the number of integration points in sections with limited inelastic response. The proposed scheme is presented for circular and rectangular cross sections, but the approach is applicable to other section shapes. Inelastic frame response examples demonstrate the benefits of the proposed discretization scheme for the nonlinear response history analysis of large structural models.

INTRODUCTION

Fiber beam/column elements with fiber section discretization are widely used for the simulation of the inelastic response of building and bridge models, because they represent a good compromise between accuracy and computational efficiency for assessing the global and local response of steel, concrete and composite frame models (Kostic and Filippou 2012; Terzic and Stojadinovic 2015;

Hajjar et al. 1998). Regardless of the type of frame element formulation (Neuenhofer and Filippou 1997; Kostic and Deretic-Stojanovic 2016; Scott and Fenves 2006), the inelastic deformations are monitored at two or more integration points (sections) along the element. Each monitoring section is discretized into integration points (fibers) with a uniaxial or multi-axial material stress relation. The numerical integration over the cross section gives the section forces s and the stiffness matrix $\mathbf{k}_s$, which are then integrated over the element to give the element response to given displacements.

In professional practice the modeling of frames favors elements with concentrated plastic hinges at the ends in adherence with the guidelines for the nonlinear evaluation of structural response (ASCE-41). Furthermore, a frame element with concentrated plastic hinges is computationally efficient than an element with a fiber discretization of the cross section, despite its shortcomings of accuracy and numerical robustness, especially for reinforced concrete (RC) and composite structural elements undergoing large inelastic deformations. An important factor for the relative computational efficiency of the plastic hinge model over the fiber section model is the tendency to use a large number of fibers in the latter in an excessive zeal for accuracy and in fear of numerical instabilities. Because the computational time and data storage requirements for the response determination of large structural models increases almost proportionally with the number of fibers in the section discretization, the selection of an optimum number of fibers becomes important.

A few past studies have investigated the efficient integration of the section response. These studies can be divided into two groups. The first group deals with the formulation of heuristic rules for an efficient section discretization scheme. Berry and Eberhard (2008) proposed rules for the efficient discretization of circular reinforced concrete bridge piers with regular circular meshes. Kostic and Filippou (2012) studied different integration rules and proposed efficient fiber meshes for the discretization of wide flange steel sections and rectangular RC sections. The study concludes that higher order integration rules do not offer accuracy benefits over the simple midpoint integration rule for the cyclic inelastic response of homogeneous or inhomogeneous sections. Tao and Nie (2015) studied the discretization of composite steel/concrete beams and columns and proposed a few discretization schemes. Recently, Cohen et al. (2022) proposed several schemes for the efficient discretization of circular reinforced concrete sections using meshes with a variable number of fibers that increase with distance from the center. These schemes aim to overcome the shortcomings of standard discretization schemes that result in many fibers of very small area near the center of the circular section where they play a minor role in the response evaluation. The study by Cohen et al. (2022) also proposes consistent error measures for the selection of a suitable discretization scheme on the basis of accuracy criteria.

The second group of past studies deals with adaptive discretization strategies. In this context He et al. (2017a) and He et al. (2017b) assume that all control sections of a nonlinear beam-column element are linear elastic at the start of the analysis. When the deformations at a control section exceed specified limit values, a standard fiber discretization is used for evaluating the inelastic response of the particular section. The adaptive scheme by Song et al. (2000) and Izzuddin and Lloyd Smith (2000) is concerned with the discretization of the beam-column element along its length. An elaborate scheme is proposed for detecting the onset of inelastic strains in a beam-column element under the interaction of axial force and bending moment.

The present study belongs to the group of adaptive schemes and uses cubature rules (Cools 2003) for the exact integration of the section response in the linear elastic range. Once inelastic deformations arise at a particular section, the proposed scheme introduces integration points at the particular section following the spread of the inelastic strains into the section core. This approach ensures an optimum balance between accuracy and computational efficiency. In contrast to the proposal by He et al. (2017b), the proposed scheme uses a gradual mesh refinement of the section with increasing inelastic deformation, thus ensuring a smooth state transition for increased numerical robustness and computational efficiency.

After the description of the proposed adaptive scheme, the paper demonstrates its benefits with a few examples of the inelastic static and dynamic response of frames with members of homogeneous or composite, circular or rectangular cross sections.

ADAPTIVE DISCRETIZATION SCHEME

The numerical efficiency and accuracy of the inelastic section response evaluation depends on the integration rule and the number of integration points (IPs). The following proposal for the section discretization is motivated by two considerations:

- Inelastic deformations arise only at a few critical sections of the structural model, some appearing early and others late in the response history. A large portion of the monitoring sections remain in the linear elastic range during the entire response history.
- When inelastic strains arise at a critical section, they spread gradually from the edges to the center with increasing section deformation. A portion of the cross section remains in the linear elastic range.

For a homogeneous section in the linear elastic range the tangent material modulus E_t is constant. Under the assumption that plane sections remain plane the normal strains are linearly distributed and the following integrals over the section area A for determining the section stiffness $\mathbf{k}_s$ and the section stress resultants $\boldsymbol{s}$ involve at most quadratic polynomials in y and z

$$\mathbf{k}_s = \int_A E_t \begin{bmatrix} 1 & -y & z \\ -y & y^2 & -yz \\ z & -yz & z^2 \end{bmatrix} dA \approx \sum_{i=1}^{nf} E_{ti} \begin{bmatrix} 1 & -y_i & z_i \\ -y_i & y_i^2 & -y_i z_i \\ z_i & -y_i z_i & z_i^2 \end{bmatrix} A_i \tag{1}$$

$$\boldsymbol{s} = \begin{bmatrix} N \\ M_z \\ M_y \end{bmatrix} = \int_A \begin{bmatrix} 1 \\ -y \\ z \end{bmatrix} \sigma dA \approx \sum_{i=1}^{nf} \begin{bmatrix} 1 \\ -y_i \\ z_i \end{bmatrix} \sigma_i A_i \tag{2}$$

where nf is the number of fibers or IPs, σ is the normal stress, and the subscript i refers to the variables for the i-th fiber.

An exact numerical evaluation is, therefore, possible. The lowest order integration rule for quadratic polynomials requires 5 IPs for the circle and 5 IPs for the square with the location and weights in Fig. 1 (Abramowitz et al. 1965; Cools 2003).

With the underlying assumption for Euler-Bernoulli beam-column elements that plane sections remain plane, the normal strains are available everywhere in the section during the response history.It

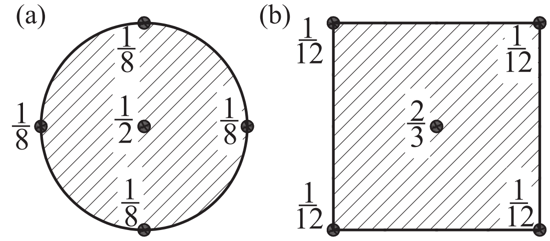

Fig. 1. Cubature rules for (a) unit area circle (5 IPs), and (b) unit area square (5 IPs)

is, therefore, easy to detect the instant when the largest positive or negative normal strain exceeds a specified limit so as to modify the discretization of the portion of the section that experiences inelastic strains.

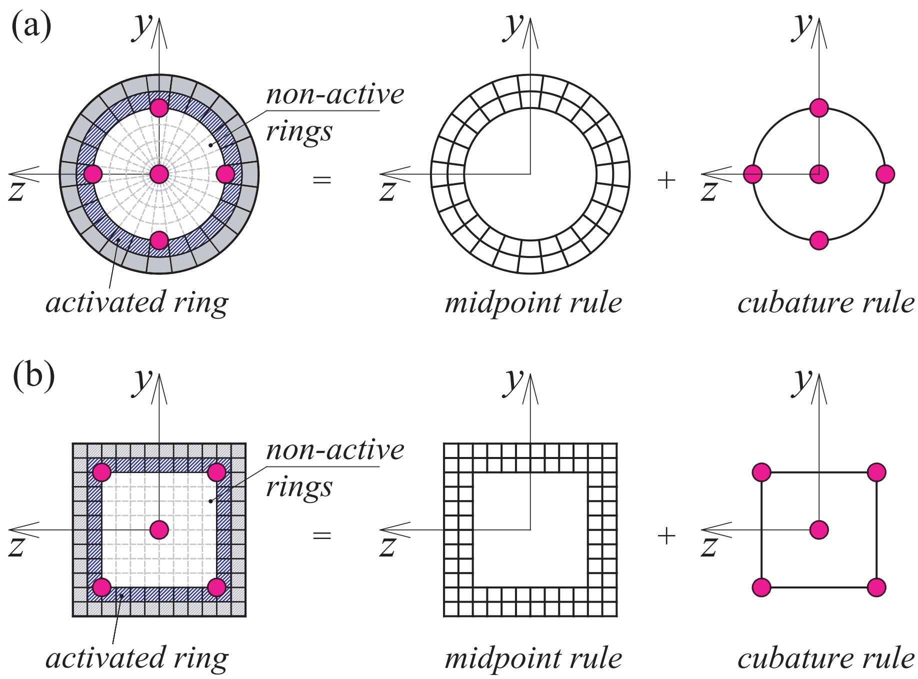

Fig. 2. Adaptive discretization for two section geometries after second ring activation

Fig. 2 is a schematic depiction of the concept for a circular and a rectangular section: starting from a target final discretization mesh shown with light gray lines, Fig. 2(a) shows the activation of the second ring from the perimeter once the trigger condition is met at the control location. The section response at this state uses the midpoint integration rule for the outermost ring in medium gray and for the newly activated ring in blue-gray color, while the elastic core is integrated with the cubature rule of 5 IPs. A similar scheme is used for the rectangular section in Fig. 2(b) where the "rings" are of rectangular tubular form. The final discretization for the rectangular and for the circular section in Fig. 2 is based on the recommendations of earlier studies (Kostic and Filippou 2012) and (Cohen et al. 2022), respectively.

The criterion for the activation of a new ring or a rectangular tube under biaxial bending conditions depends on the identification of the extreme normal strain for homogeneous sections or of the largest positive or negative strain for composite sections, whichever is more critical.

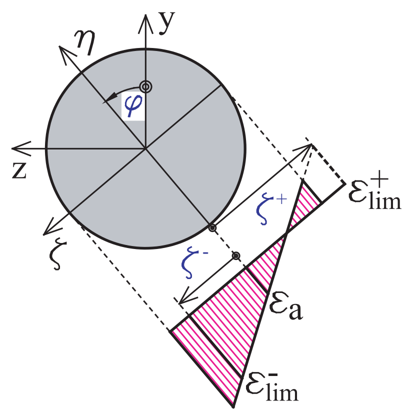

Fig. 3. Coordinate system rotation

The determination of the extreme normal strain is based on the following process: for the given section deformations **e**

$$\mathbf{e} = \begin{bmatrix} \epsilon_a \\ \kappa_z \\ \kappa_y \end{bmatrix} \tag{3}$$

where ϵ_a is the normal strain at the origin of the section coordinate system, κ_z the curvature about the z-axis, and κ_y the curvature about the y-axis, the orthogonal coordinate system (η, ζ) is introduced in Figure 3 with angle φ relative to the reference coordinate system (y, z) of the structural model where

$$\tan\varphi = \frac{\kappa_z}{\kappa_y}. \tag{4}$$

The following relation holds between the coordinates of a point in the two systems

$$\begin{bmatrix} y \\ z \end{bmatrix} = \begin{bmatrix} \cos\varphi & -\sin\varphi \\ \sin\varphi & \cos\varphi \end{bmatrix} \begin{bmatrix} \eta \\ \zeta \end{bmatrix} \tag{5}$$

The relation between the normal strain ε and the section deformations **e** is given by the assumption of plane sections remaining plane after deformation

$$\varepsilon = \epsilon_a - y\,\kappa_z + z\,\kappa_y \tag{6}$$

By replacing the coordinates y and z in Eq (6) with the relations from Eq (5) and noting the definition of the angle φ from Eq (4), it is possible to reduce the dependence of the normal strain to a single curvature κ_η about the η-axis (Zupan and Saje 2005)

$$\varepsilon = \epsilon_a + \kappa_\eta\,\zeta \tag{7}$$

where

$$\kappa_\eta = \kappa_z\,sin\varphi + \kappa_y\,cos\varphi \tag{8}$$

Eq (7) gives the distances ζ^- and ζ^+ from the origin of the coordinate system to the location where the normal strain ε reaches the negative limit value ε_{lim^-} and the positive limit value ε_{lim^+}, respectively (Figure 3). A ring is activated when the smaller distance ζ_{min} exceeds the outer, the inner, or the mid-radius of the next ring of the section discretization.This study uses the mid-radius of the next ring. If one ζ value falls outside the section, as Fig. 3 shows for ζ^+, the corresponding strain limit (ε_{lim^+}) is not critical. When both ζ values fall outside the section, the discretization does not change.

The strain limit for the ring activation is flexible: it can be either related strictly to the onset of a well defined limit state for the material, e.g. the yield strain of the steel, or, it can be specified in terms of a critical value. The examples will show that there is some leeway in the selection of the triggering strain limit depending on the target response accuracy.

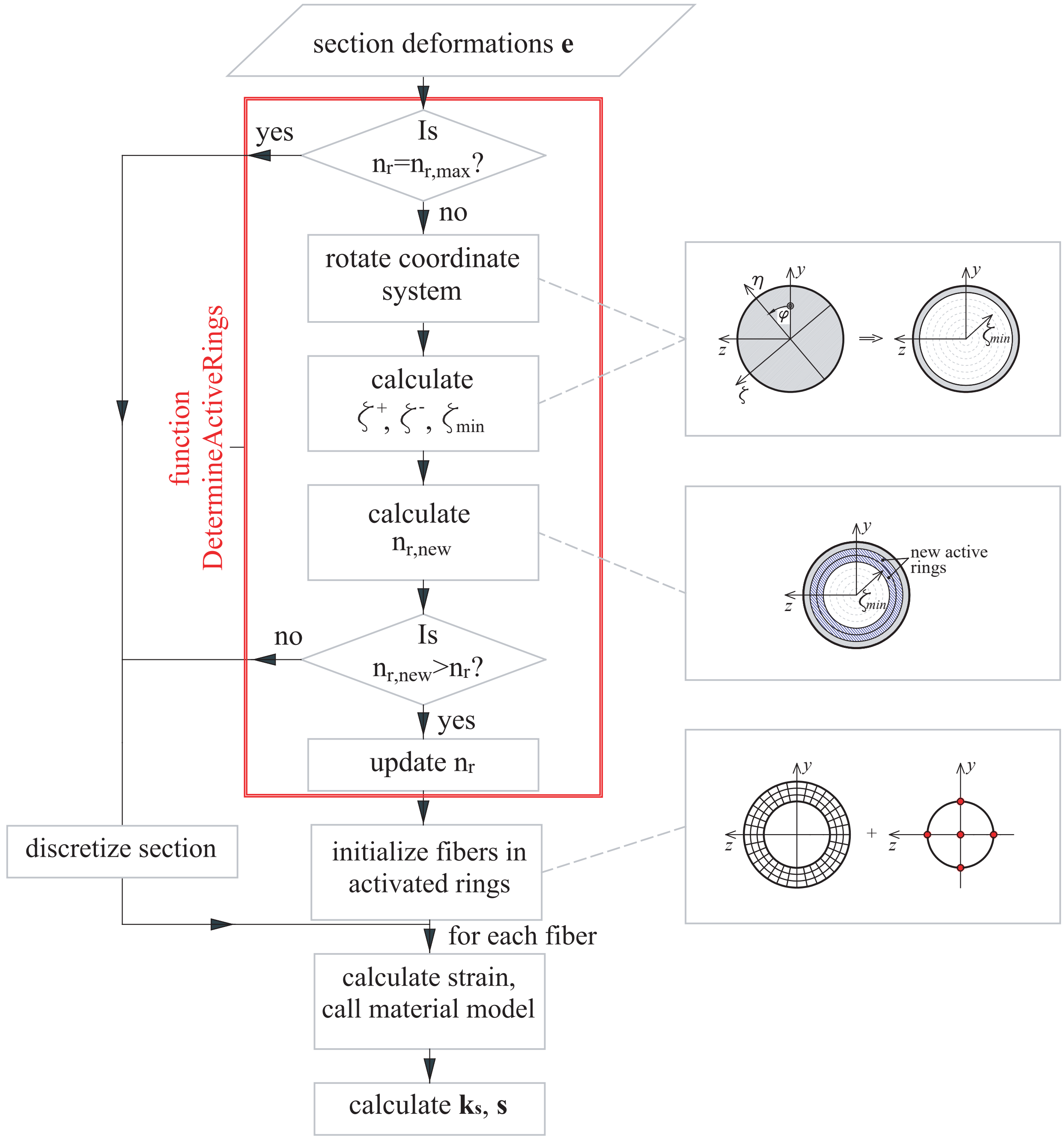

Fig. 4. Flowchart of adaptive section discretization algorithm for a circular cross-section

Fig. 4 provides a schematic summary of the adaptive section discretization algorithm. The first group of commands concerns the determination of the number n_r of active rings. These are enclosed with a red outline in Fig. 4. As long as n_r is smaller than the total number of rings $n_{r,max}$

for the target final section discretization, the section deformations $\mathbf{e}$ are used to set up the coordinate system (η, ζ) and determines the curvature κ_η and the distances ζ^- and ζ^+. The next step establishes the distance ζ_{min} with $\zeta_{min} = \min(\zeta^-, \zeta^+)$ for the target limit strain and determines the number of rings $n_{r,new}$ to be activated. If $n_{r,new} > n_r$, the value of n_r is updated. After establishing the number of active rings, the section state determination of the stiffness $\mathbf{k_s}$ and the resisting forces $\mathbf{s}$ uses the the midpoint integration rule over the activated rings and the cubature rule over the remainder of the section. For the implementation of the algorithm in a general purpose analysis framework, the steps inside the red outline of Fig. 4 are performed by a function that precedes the section state determination and determines the number n_r of active rings based on the specified data $n_{r,max}$, and $[\, \varepsilon_{lim^-}\,,\ \varepsilon_{lim^+}\,]$. With the established discretization, the general purpose section state determination module returns the stiffness $\mathbf{k_s}$ and the resisting forces $\mathbf{s}$ for the given deformations $\mathbf{e}$.

The implementation of the algorithm into a general analysis framework (such as OpenSees) requires modifications at the section level but not at the material or at the element level. A new parent class for the sections with adaptive discretization is necessary with child classes for the section geometry: rectangular, circular, etc. Each child class has, besides n_r, $n_{r,max}$ and the trigger strain values $[\, \varepsilon_{lim^-}\,,\ \varepsilon_{lim^+}\,]$, its own attributes for describing any intermediate and the final section discretization. In addition, each child class has its own procedure for determining the activated region of the adaptive discretization scheme for the particular shape.

In the following, the proposed adaptive discretization is applied to circular and rectangular sections of a single material, or of composite type, such as reinforced concrete (RC) or concrete filled tube (CFT) sections. The scheme can be readily extended to other section geometries by dividing the section into a number of constituent basic shapes with an available cubature rule for the homogeneous case with constant properties and specifying the final fiber discretization of each shape.

For the section analyses the reinforced concrete sections are divided into two parts: the cover with a uniaxial stress-strain relation for unconfined concrete, and the core with a uniaxial relation for confined concrete. From the conclusions of a recent study Cohen et al. (2022) on circular RC sections a single ring suffices for the discretization of the concrete cover for all practical purposes. The present study extends this conclusion to circular CFT sections and rectangular RC and CFT sections based on the results of an earlier study by Kostic and Filippou (2012). Consequently, the adaptive discretization is limited to the confined concrete core for either RC or CFT section type.

EVALUATION OF RING ACTIVATION CRITERIA

The accuracy and computational efficiency of the adaptive section discretization depends on the strain limit for the activation. The closer the strain limits [ε_{lim^-} and ε_{lim^+}] are to the onset of inelastic material behavior the more accurate is the section state determination, but the gain of computational efficiency is correspondingly smaller. Relaxing the trigger strain for ring activation increases the computational efficient at the expense of accuracy. It is, therefore, interesting to explore the balance between accuracy and computational efficiency for the adaptive discretization scheme by studying a few trigger strain alternatives. Ultimately, the choice also depends on the size of the structural model and the target accuracy for the determination of the global displacements and the local deformations of the structural model, which should be left to the discretion of the analyst.

For materials with a well defined linear range with yield strength f_y and elastic modulus E it is reasonable to set the trigger strain values [ε_{lim^-} , ε_{lim^+}] equal to [$-\frac{f_y}{E}$, $\frac{f_y}{E}$], respectively. For concrete which exhibits different behavior in tension than in compression and which does not possess a well defined linear range in compression, this study investigates three alternatives for the trigger strain values. The first is denoted with $e_{lim,1}$ and uses the range $e_{lim,1} = [\, 0.25\, \varepsilon_{co} \,,\, \frac{f_t}{E_c}\,]$ where ε_{co} is the strain at the compressive strength, E_c is the initial tangent modulus, and f_t is the tensile strength. This is the most stringent ring activation criterion that is suitable for the representation of the initial stiffness of RC members and its evolution under small inelastic excursions. The second alternative is denoted with $e_{lim,2}$ and relaxes the target compressive strain so that $e_{lim,2} = [\, \varepsilon_{co} \,,\, \frac{f_t}{E_c}\,]$. Finally, the third alternative is denoted with $e_{lim,3}$ and removes the target tensile strain from the ring activation criterion so that $e_{lim,3} = [\, \varepsilon_{co} \,,\, - \,]$. Both options are suitable for RC members undergoing large inelastic excursions for which the focus is on the accurate determination of the inelastic deformations and strains rather than of the initial stiffness.

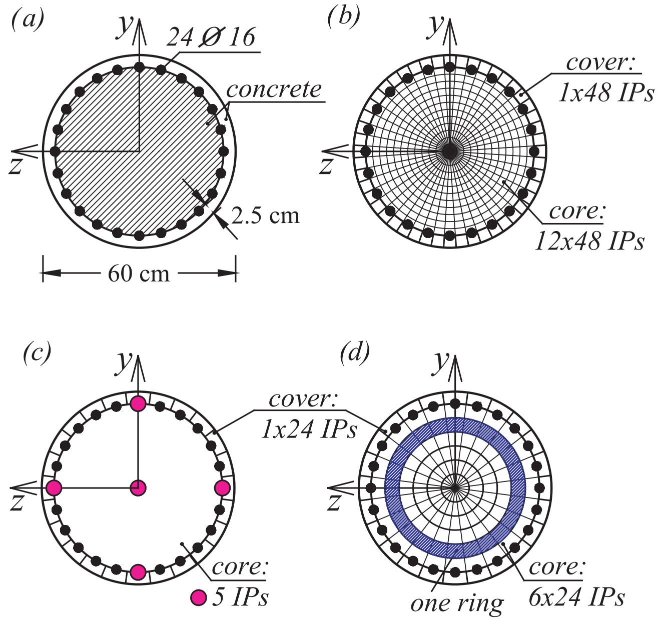

Fig. 5. RC cross section (a) dimensions; (b) reference discretization; (c) discretization at the start of the analysis, and (d) final discretization with all rings activated

The following examples assess the effect of the target strain limit alternatives on the response of a circular RC section and a rectangular CFT section.

Fig. 5 shows the geometry of the RC section in (a), the reference discretization for the "numerically exact" response in (b), the discretization at the start of the analysis is (c), and the final discretization with all rings activated in (d).

Fig. 6 shows the geometry of the CFT section in (a), the reference discretization for the "numerically exact" response in (b), the discretization at the start of the analysis is (c), and the target discretization with all rings activated in (d)

The RC section is subjected to the circular curvature history in Fig. 7(a) under a constant axial force. The CFT section is subjected to the clover leaf curvature history in Fig. 7(b) under a variable axial force with values ranging between $-0.48N_u$ and $+0.08N_u$, where N_u is the axial compression capacity of the section.

The RC section is subjected first to an axial compression of 40% of the ultimate compression strength N_u that is maintained constant during the curvature history. Following the application of

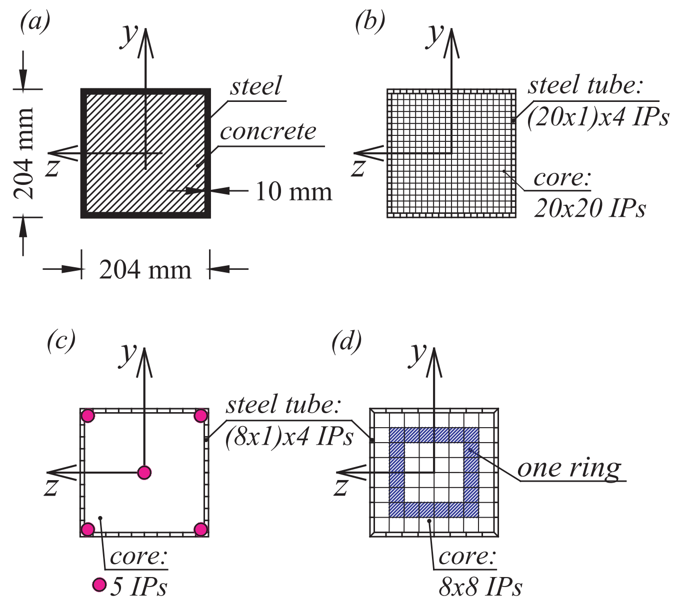

Fig. 6. CFT cross section (a) dimensions; (b) reference discretization; (c) discretization at the start of the analysis, and (d) final discretization with all rings activated

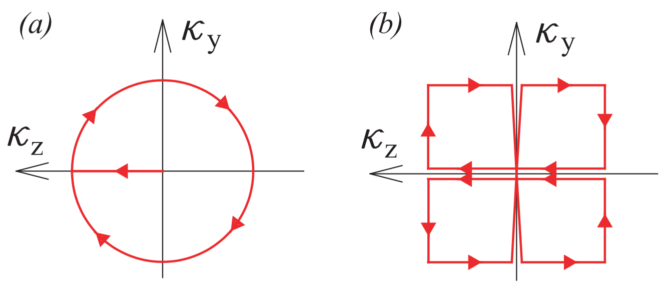

Fig. 7. Section curvature history (a) for RC section, and (b) for CFT section

the axial force, the curvature κ_z increases from 0 to the maximum value $\kappa_{z,max}$, as Fig. 7(a) shows, followed by the variation of κ_y and κ_z on a circular path. The maximum curvature values are $\kappa_{y,max} = \kappa_{z,max} = 2.8 \cdot 10^{-4}$ (1/cm), giving rise to a maximum concrete compression strain of 1‰.

The material model by (Mander et al. 1998) with linear tension stiffening is used for the uniaxial concrete stress-strain relation. The concrete compressive strength is equal to $f'_c = 34.5$MPa and the modulus of elasticity is $E_c = 27800$ MPa. For the confined concrete core a strength increase factor of $K = 1.2$ is used in the model, which also affects the descending portion of the concrete stress-strain relation in compression. The tensile strength f_t of the unconfined and the confined concrete is set equal to 3.1 MPa. The section reinforcement ratio is $\rho = 1.74\%$ with 24-ϕ16 bars in a circular pattern at 2.5 cm from the edge. The stress-strain relation of the reinforcing bars is described with the Giuffre-Menegotto-Pinto (GMP) model with yield strength f_y = 468.8 MPa, initial modulus E_s = 200 GPa, and kinematic strain hardening ratio of 0.5%. The discretization in Fig. 5(b) is used for the "numerically exact" reference solution and consists of a single ring for the concrete cover and 12 rings of equal thickness for the concrete core (n_r = 12) with n_{th} = 48 fibers in the circumferential direction for a total of 624 fibers. Fig. 5(c) shows the section discretization at the start of the analysis and gradually activates all rings of the final mesh in Fig. 5(d). This final discretization consists of one ring for the concrete cover and 6 rings of equal thickness for the concrete core (n_r = 6) with n_{th} = 24 fibers in the circumferential direction for a total of 168 fibers. In the mesh for the reference solution in Fig. 5(b) as well as in the final mesh of the adaptive discretization each reinforcing bar is represented with one fiber, thus increasing the total number by 24.

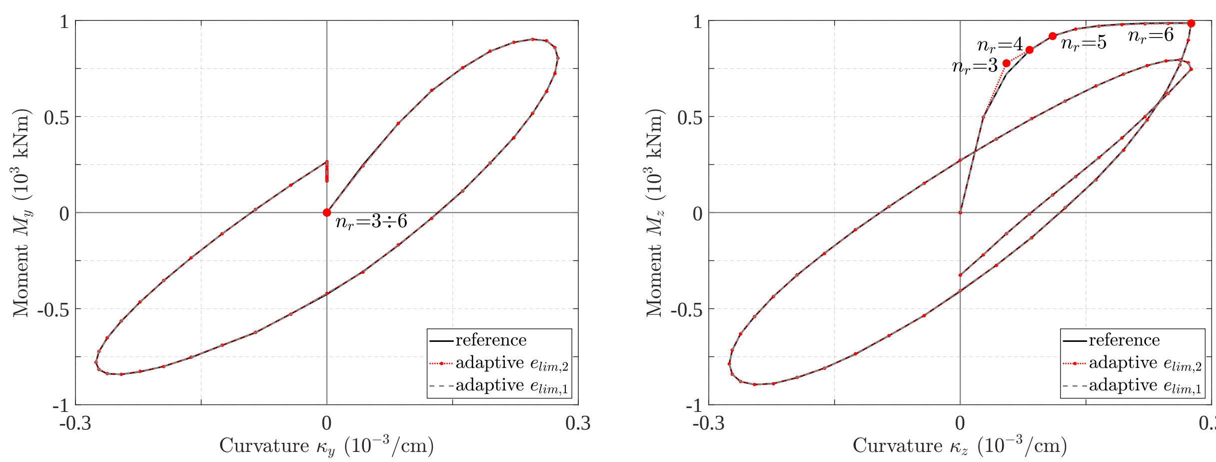

(a) Response about y-axis

(b) Response about z-axis

Fig. 8. Moment-curvature relation for the circular RC section with strain limits $e_{lim,1}$ and $e_{lim,2}$ showing the successive activation of the 6 rings for the final discretization of Fig. 5(d)

Fig. 8 and Fig. 9 show the moment-curvature relations for the circular RC section under the cycle of the circular curvature history in Fig. 7(a). The reference solution in both figures results from the fine mesh in Fig. 5(b). Fig. 8 compares the adaptive discretization response with strain limits $e_{lim,1}$ and $e_{lim,2}$ with the reference solution, while Fig. 9 compares the adaptive discretization

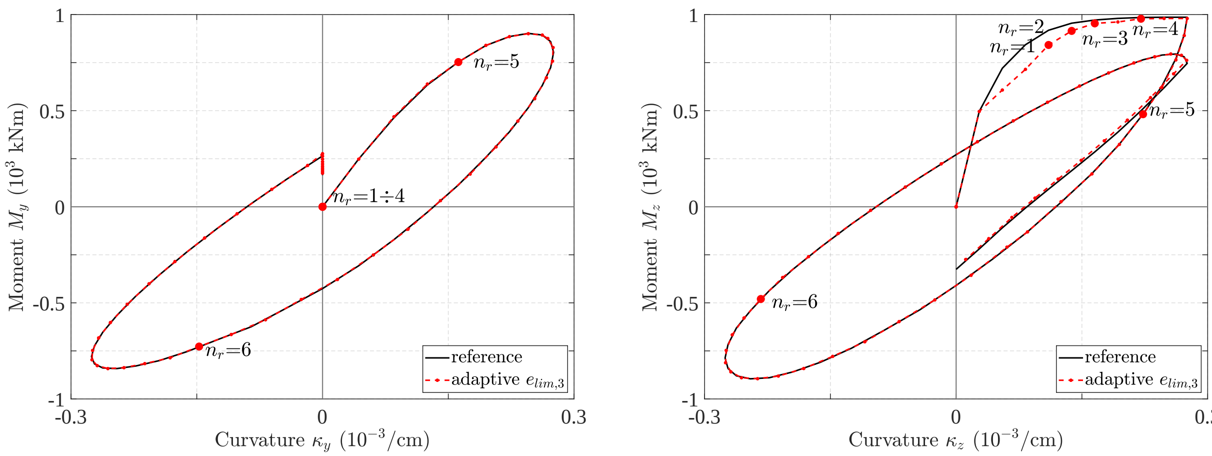

(a) Response about y-axis

(b) Response about z-axis

Fig. 9. Moment-curvature relation for the circular RC section with strain limits $e_{lim,3}$ showing the successive activation of the 6 rings for the final discretization of Fig. 5(d)

response with strain limits $e_{lim,3}$ with the reference solution.

The results of the adaptive discretization with the strict strain range $e_{lim,1}$ are practically indistinguishable from the reference solution in Fig. 8. The adaptive discretization with the more flexible strain range $e_{lim,2}$ deviates slightly from the reference solution in Fig. 8(b) during the transition from the initial response to the yield initiation in the outer rings of the section mesh. Mostly the response is again indistinguishable from the reference solution. The response with the adaptive discretization with the strain range $e_{lim,3}$ in Fig. 9 which does not include a trigger strain for ring activation under concrete cracking deviates significantly from the reference solution in the transition from the initial response to the curvature range with almost constant moment M_z in Fig. 9(b), but is again practically indistinguishable from the reference solution for the remainder of the response about the z-axis in Fig. 9(b) and for the entire response about the y-axis in Fig. 9(a). Fig. 8 and Fig. 9 mark the instant of each ring activation for the adaptive solutions with $e_{lim,2}$ and $e_{lim,3}$, respectively.

Fig. 8 shows that all rings activate during the first phase of the loading history with the increase of the curvature κ_z from 0 to its maximum value. In contrast, Fig. 9 (a) and (b) shows that only 4 of the 6 rings activate during this phase, while the other two activate during the circular loading path.

Comparing the instant for each ring activation between Fig. 8 and Fig. 9 reveals that the tensile cracking strain controls the ring activation in Fig. 8 while the compressive strain ε_{co} controls the ring activation in Fig. 9, which takes place significantly later in the response history. These results lead to the conclusion that ignoring the tensile cracking strain in the ring activation criterion reduces the computational cost of the analysis but affects the accuracy of the response during the transition from the initial response to the significant spread of inelastic strains. While this limitation may not be significant for the static pushover analysis of structural models, it may affect the accuracy of the dynamic response under moderate ground excitations, as subsequent examples will show.

The rectangular CFT section in Fig. 6(a) is subjected to a single cycle with the clover leaf curvature history in Fig. 7(b) with maximum curvature values of $\kappa_{y,max} = \kappa_{z,max} = 4 \cdot 10^{-4}$ (1/cm). The CFT section is subjected to a variable axial force with values ranging between $-0.48\,N_u$ and $+0.08\,N_u$, where N_u is the axial compression capacity of the section.

The material model by (Mander et al. 1998) with linear tension stiffening is used for the uniaxial concrete stress-strain relation. The concrete compressive strength is equal to f'_c = 30.2MPa and the modulus of elasticity is E_c = 27800 MPa. For the concrete confined by the steel tube a strength increase factor of $K = 1.3$ is used in the model, which also affects the descending portion of the concrete stress-strain relation in compression. The tensile strength f_t of the concrete is equal to 3.1 MPa. The stress-strain relation of the steel tube is described by the GMP model with yield strength f_y = 291 MPa, initial modulus E_s = 200 GPa, and kinematic strain hardening ratio of 0.5%.

The discretization in Fig. 6(b) is used for the "numerically exact" reference solution and consists of a mesh of 20x20 concrete fibers with a single fiber across the thickness of the steel tube for a total of 480 fibers. The section discretization at the start of the analysis in Fig. 6(c) evolves to the final mesh in Fig. 6(d) when the section deformations are so large as to activate all tubular "rings". The final discretization uses a mesh of 8x8 concrete fibers with a single fiber across the thickness of the steel tube for a total of 96 fibers.

Fig. 10 and Fig. 11 show the moment-curvature relations for the rectangular CFT section under the cycle of the clover leaf curvature history in Fig. 7(b). The reference solution in both figures

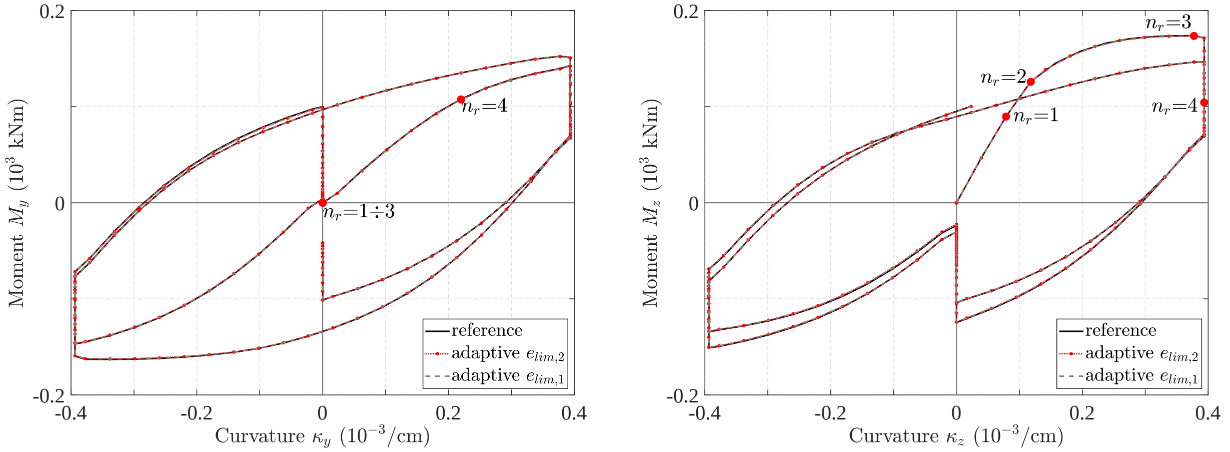

(a) Response about y-axis

(b) Response about z-axis

Fig. 10. Moment-curvature relation for the rectangular CFT section with strain limits $e_{lim,1}$ and $e_{lim,2}$ showing the successive activation of the 4 rings for the final discretization in Fig. 6(d)

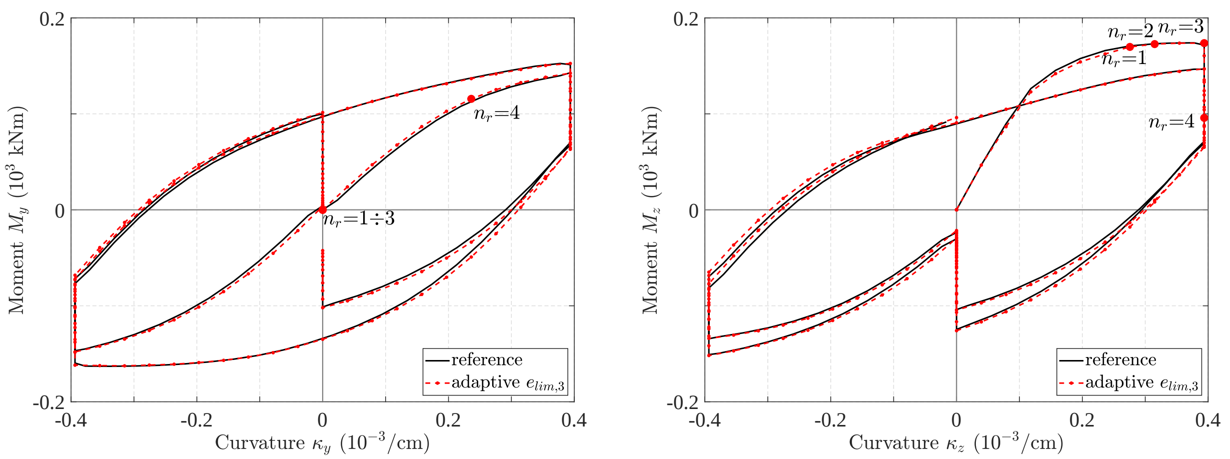

(a) Response about y-axis

(b) Response about z-axis

Fig. 11. Moment-curvature relation for the rectangular CFT section with strain limits $e_{lim,3}$ showing the successive activation of the 4 rings for the final discretization in Fig. 6(d)

results from the fine discretization in Fig. 6(b). The response with the adaptive discretization with strain limits $e_{lim,1}$ and $e_{lim,2}$ are compared with the reference solution in Fig. 10 and the response with adaptive discretization with strain limits $e_{lim,3}$ is compared with the reference solution in Fig. 11. The response with the adaptive discretization with strain limits $e_{lim,1}$ and $e_{lim,2}$ is again practically indistinguishable from the reference solution in Fig. 10, while the adaptive discretization with strain limits $e_{lim,3}$ exhibits a very small strength difference for the entire response starting with the onset of yielding in Fig. 11.

Comparing the activation instant of each tubular "ring" between Fig. 10 and Fig. 11 shows that the activation delay for the trigger strain criterion without the tensile cracking strain is appreciable only for the first two tubular "rings". Because the corresponding inelastic curvature range is large, the more flexible trigger strain criterion is expected to offer computational benefits for the static and dynamic response of large scale models under moderate excitations.

The conclusion from these section analyses is that the ring activation with trigger strain limits $e_{lim,2}$ gives results of excellent accuracy for the entire response under a biaxial curvature history cycle with constant or variable axial force. The ring activation with trigger strain limits $e_{lim,3}$ that do not include the concrete cracking strain holds significant promise for reducing further the computational cost of the adaptive section discretization, but has accuracy limitations during the transition between the initial response and significant spread of yielding. The effect of this accuracy limitation on the global and local response of structural models will be studied in the next section. Irrespective of the ring activation criterion the proposed adaptive scheme optimizes the number of section integration points for the inelastic response of fiber beam-column elements and is characterized by the smooth transition from one ring activation to the next in contrast to the abrupt change from the elastic to the inelastic response state (He et al. 2017b). This characteristic bodes well for the numerical robustness of the scheme for the inelastic response simulation of large structural models.

RESPONSE OF STRUCTURAL MODELS

The next section assesses the computational cost benefit of the proposed adaptive discretization scheme for the inelastic dynamic response simulation of a 3d RC frame and for the nonlinear dynamic and pushover analysis of a 2d composite frame. The numerical simulations were conducted with FEDEASLab, a general purpose framework for nonlinear structural analysis based on Matlab (Filippou and Constantinides 2004).

3d Reinforced Concrete Frame

The first structural model example concerns the inelastic dynamic response simulation of the 3-story reinforced concrete frame in Fig. 12 from the study by He et al. (2017a). In the present study the beam cross section is assumed to be rectangular and the total mass of 10 t is uniformly divided and lumped at the nodes. The 3-story frame is subjected first to gravity loads of 400 kN at the top of each column followed by a bidirectional earthquake excitation in the X and Y direction of Fig. 12 with the acceleration record at the Takatori station from the 1994 Kobe earthquake. The original earthquake record with a peak ground acceleration (PGA) of 0.618g gives rise to large inelastic deformations. The earthquake record is scaled to PGA values of 0.4g and 0.15g for studying the effectiveness of the adaptive section discretization under moderate ground excitations. The model of this study uses a single fiber beam-column element for each member of the 3d RC frame. The element uses the force formulation with 4 Gauss-Lobatto IPs for each column and 5 IPs for each girder. The nonlinear geometry under large displacements is taken into account with the corotational formulation. The structural model assumes that the floor slabs form a rigid diaphragm in their plane.

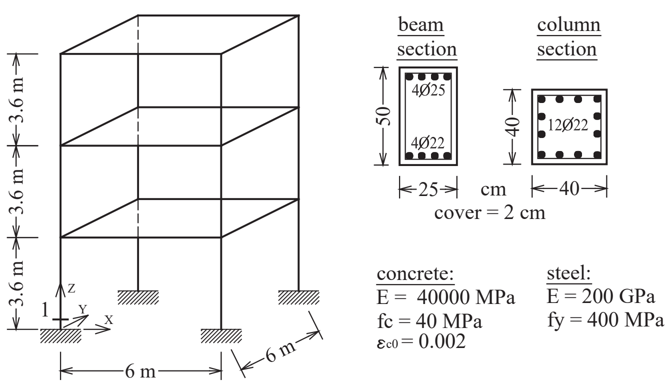

Fig. 12. Three story RC frame

Fig. 12 lists the material properties for the concrete and the reinforcing steel. The confinement of the core concrete in the columns and the girders is accounted for with a strength increase factor of $K = 1.2$ in the material model by (Mander et al. 1998). The GMP model is used for the reinforcing steel with a kinematic strain hardening ratio of 0.2%. The reference section discretization for the "numerically exact" response uses a single fiber across the cover thickness with 10 fibers on each side and a 10x10 fiber mesh for the concrete core. The final discretization of the adaptive scheme uses the recommendations of the study by Kostic and Filippou (2012) with 8 fibers on each side of the concrete cover with a single fiber across the cover thickness and with an 8x8 fiber mesh for the concrete core. The portion of the cross section with maximum strain less than the trigger value for ring activation is integrated with the cubature rule in Fig. 1(b). The trigger strain values for ring activation are based on the strain ranges $e_{lim,2}$ and $e_{lim,3}$, as defined earlier.

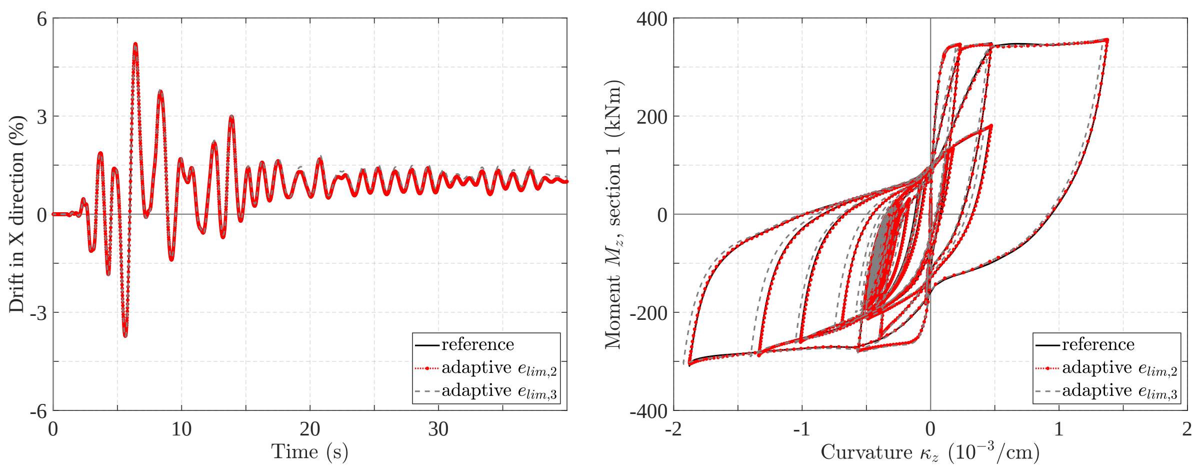

(a) Roof drift history in X direction (b) Moment-curvature history at column base

Fig. 13. RC frame response under the Takatori Station acceleration record with PGA of 0.618g

Because the frame and the loading are symmetric, it suffices to investigate the structural response in one principal direction. Fig. 13 shows the roof drift history in the X-direction and the moment-curvature response at the base of the first story column for the Takatori Station record with a PGA of 0.618g. The results of the adaptive section discretization scheme with both trigger strain alternatives match almost perfectly those of the reference solution with a very slight difference between the adaptive solution with the trigger strain criterion $e_{lim,3}$ and the reference solution for the moment-curvature relation in Fig. 13(b). The excellent accuracy of both adaptive discretization schemes is noteworthy given the several cycles of large inelastic deformations under this earthquake excitation before the response settles to at a residual roof drift of slightly higher than 1%.

Fig.14 shows the activation history for the sections of the beam-column elements and the tubular

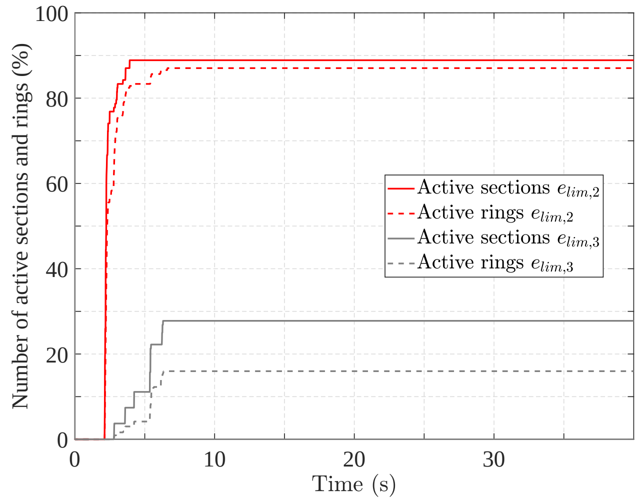

Fig. 14. Section and ring activation history for RC frame under EQ record with PGA of 0.618g *(with 100% corresponding to all monitored frame sections and to all rings in these sections)*

"rings" of each section for the adaptive discretization scheme with the trigger strain alternatives $e_{lim,2}$ and $e_{lim,3}$. Because the ring activation criterion with trigger strain limits $e_{lim,2}$ includes the tensile cracking strain, even control sections away from the inelastic zones are activated. Consequently, a very large percentage of 89% of all monitored sections in the structural model are activated during the large inelastic excursion under the base excitation with PGA of 0.618g. Among all sections a very large percentage of 87% of the tubular "rings" are activated. The fact that the activation percentage values for sections and tubular "rings" are almost the same shows that all 4 tubular "rings" are activated in the active sections of the frame elements. By excluding the tensile cracking strain from the ring activation criterion, as is the case with the trigger strain alternative $e_{lim,3}$, the percentage of active sections reduces significantly and is limited to those at the inelastic zone of the frame elements, i.e. at most 2 out of 4 IPs for the columns and at most 2 of 5 IPs for the girders. At the same time the percentage of active tubular "rings" also drops to slightly more than half of the total number in these sections meaning that on average slightly more than 2 out of 4 "rings" are activated. A detailed study of the results reveals that only 2 sections show activation of all four tubular "rings", as opposed to 92 sections for the trigger strain limits $e_{lim,2}$.

Table 1 shows that the reduction of active sections and tubular "rings" reduces the computation

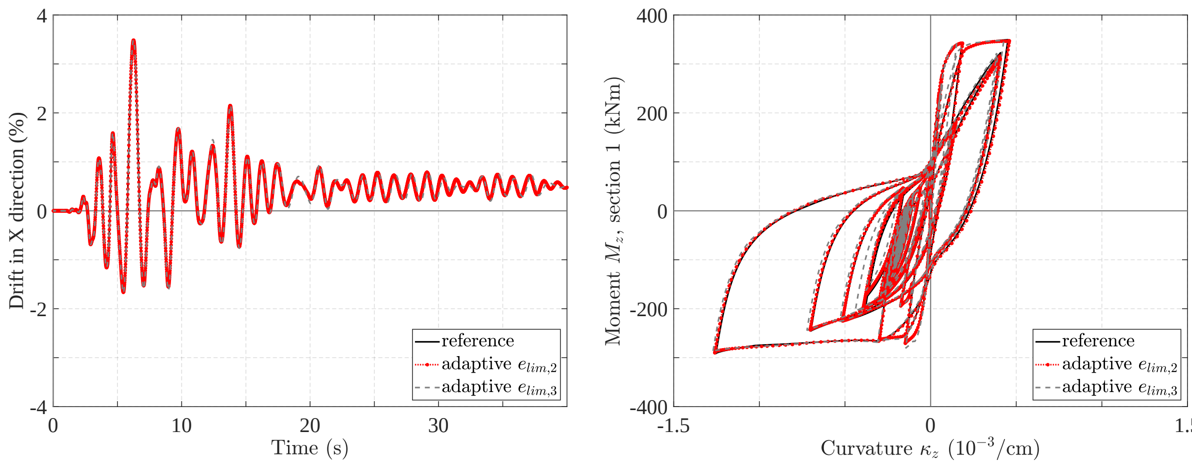

(a) Roof drift history in X direction

(b) Moment-curvature history at column base

Fig. 15. RC frame response under the Takatori Station acceleration record with PGA of 0.4g

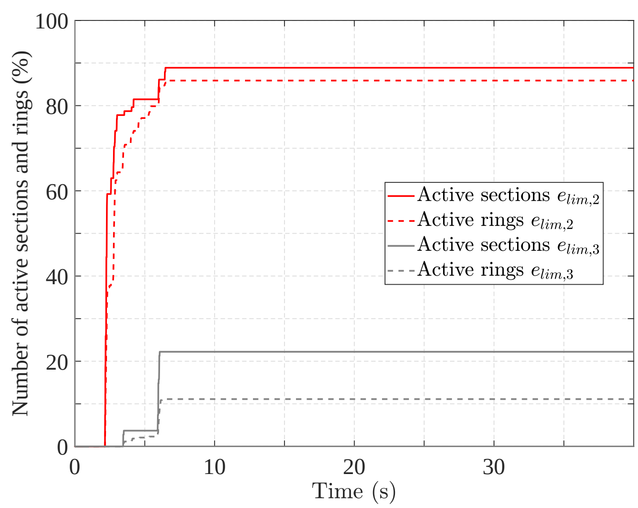

Fig. 16. Section and ring activation history for RC frame under EQ record with PGA of 0.4g

time of the inelastic response for the 3d RC frame by 32% relative to the reference solution for the trigger strain limits $e_{lim,2}$ and by 57% relative to the reference solution for the trigger strain limit $e_{lim,3}$.

Fig. 15 shows the roof drift history in the X-direction and the moment-curvature response at the base of the first story column under the Takatori Station acceleration record with a PGA of 0.40g. Fig. 16 shows the activation history for the sections and the tubular "rings" in each section of the frame elements for the adaptive discretization scheme with the trigger strain limits $e_{lim,2}$ and $e_{lim,3}$.

Because the maximum roof drift is relatively large even under this excitation, the conclusions about the adaptive discretization scheme with trigger strain limits $e_{lim,2}$ and $e_{lim,3}$ are the same as those for the acceleration record with a PGA of 0.618g. The reduction of the active tubular "rings" for the trigger strain limit $e_{lim,3}$ in Fig. 16 to 11% of the total number is more significant that for the acceleration record with a PGA of 0.618g, but this has a small impact on the computation time in Table 1.

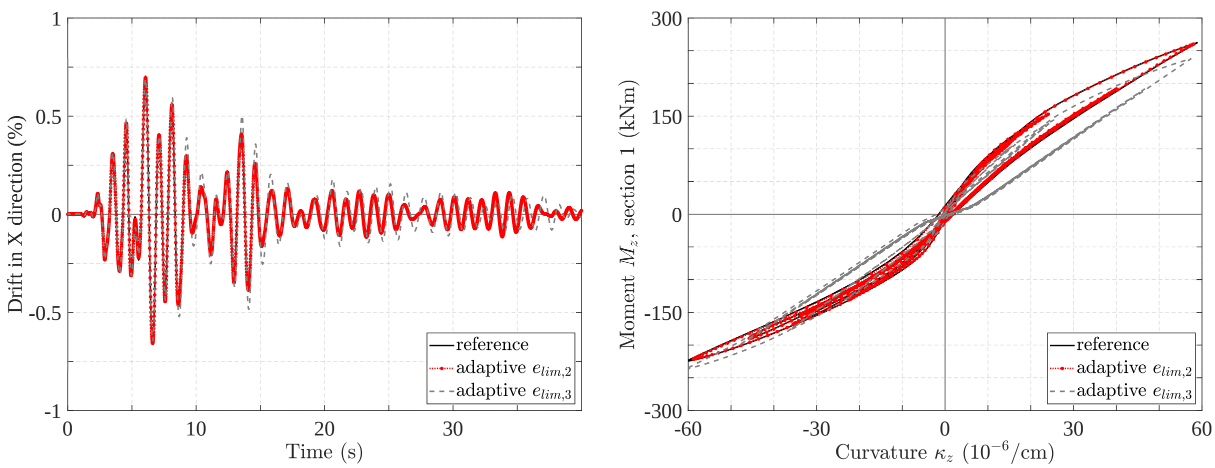

(a) Roof drift history in X direction (b) Moment-curvature history at column base

Fig. 17. RC frame response under the Takatori Station acceleration record with PGA of 0.15g

Fig. 17 shows the roof drift history in the X-direction and the moment-curvature response at the base of the first story column under the Takatori Station acceleration record with a PGA of 0.15g. In this case the maximum roof drift is significantly smaller than in the previous two cases without a residual drift at the end of the response history. The moment-curvature history at the base of the first story column in Fig. 17(b) shows that the section deformations are also significantly smaller than those in Fig. 15(b). For this level of base acceleration leaving out the tensile cracking strain from the ring activation criterion results in a slight loss of accuracy, as was observed for the section analysis in Fig. 9(b). If this loss of accuracy does not meet the analyst expectations, it is possible to tighten the trigger strain requirement with the use of the strain limits $e_{lim,2}$ for the columns and the strain limit $e_{lim,3}$ for the girders. For this ring activation criterion, which is denoted with $e_{lim,2/3}$, Fig. 18 shows the resulting improvement in the roof drift history and the moment-curvature history at the base of the first story column.

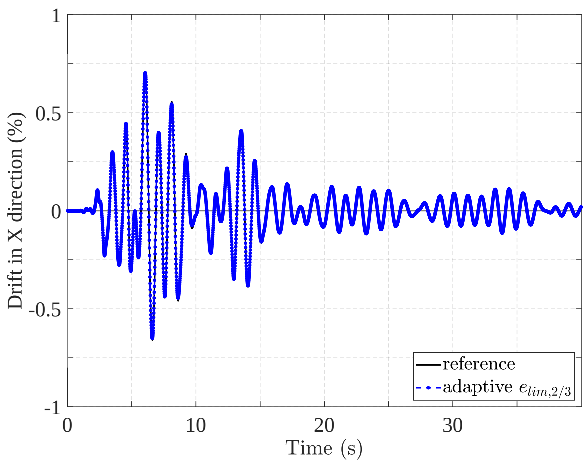

(a) Roof drift history in X direction

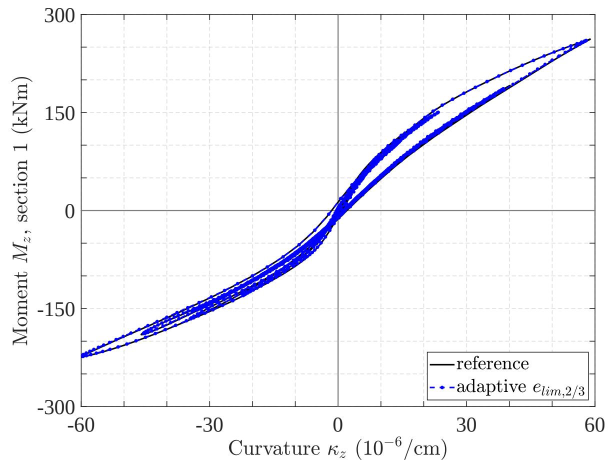

(b) Moment-curvature history at column base

Fig. 18. RC frame response under the Takatori Station acceleration record with PGA of 0.15g

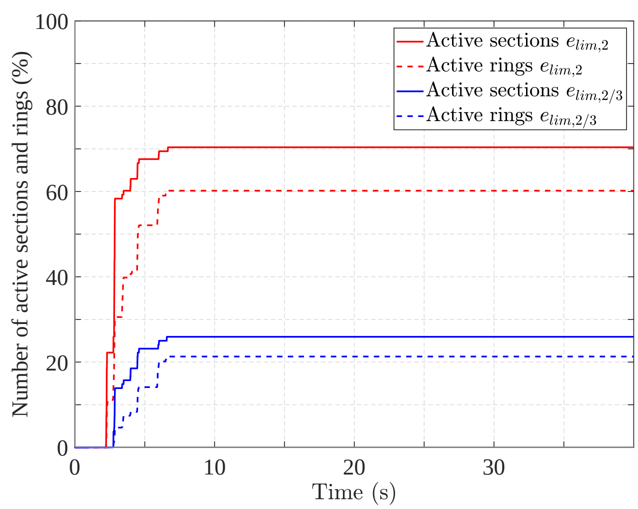

Fig. 19. Section and ring activation history for RC frame under EQ record with PGA of 0.15g

Fig. 19 shows the section and the ring activation history under the Takatori Station acceleration record with a PGA of 0.15g for the ring activation criterion with trigger strain values $e_{lim,2}$ and $e_{lim,2/3}$ while Table 1 lists the corresponding gains in computation time relative to the reference solution. The improved response accuracy in Fig. 18 with an increase of only 10% for the computation time in Table 1 leads to the conclusion that different ring activation criteria should be

TABLE 1. Calculation time for dynamic 3d RC frame analysis

Earthquake record	Reference	Adaptive $e_{lim,2}$	Adaptive $e_{lim,3}$	Adaptive $e_{lim,2/3}$
Kobe PGA 0.618g	100%	68%	43%	/
Kobe PGA 0.40g	100%	66%	40%	/
Kobe PGA 0.15g	100%	64%	35%	45%

used for the columns of the model than for the girders. Furthermore, it may be expedient to vary the ring activation criteria by structural model regions depending on their importance in the overall response.

Finally, it should be noted that the 3d section discretization scheme for the girders of the 3d RC frame is unnecessary given that these experience only a two-dimensional response.

2d Composite Frame

The second example investigates the nonlinear pushover analysis and the inelastic dynamic response of the plane composite moment frame in Fig. 20 whose design by Hu (2008) is based on the IBC 2003 (2003) and the AISC 2005 Seismic Design Provisions (2005). The objective of the earlier study was the effect of different models for the connection between the wide flange beam and the CFT column on the seismic response. This study uses the frame 4END-C7 with square CFT columns and wide flange steel beams Hu (2008) for the evaluation of the adaptive section discretization scheme without consideration of the connection panel zone. Fig. 20(b) shows the frame geometry, the cross-sections, the material properties, and the loading.

The frame is subjected to gravity loads w = 1.2DL+1.0LL, where DL = 21.89 kN/m represents the dead load, and LL = 17.51 kN/m the live load. In the nonlinear pushover analysis the gravity loads are applied first followed by incremental lateral forces with the distribution in Fig. 20(a) according to the IBC 2003 code. For the dynamic analysis the gravity loads are applied first followed by the application of the horizontal ground acceleration for the LA23 record from the 1989 Loma Prieta earthquake with a PGA of 0.42g. The mass corresponding to 1.0DL+0.2LL is lumped at the nodes of the model and the damping is assumed to be mass proportional with a

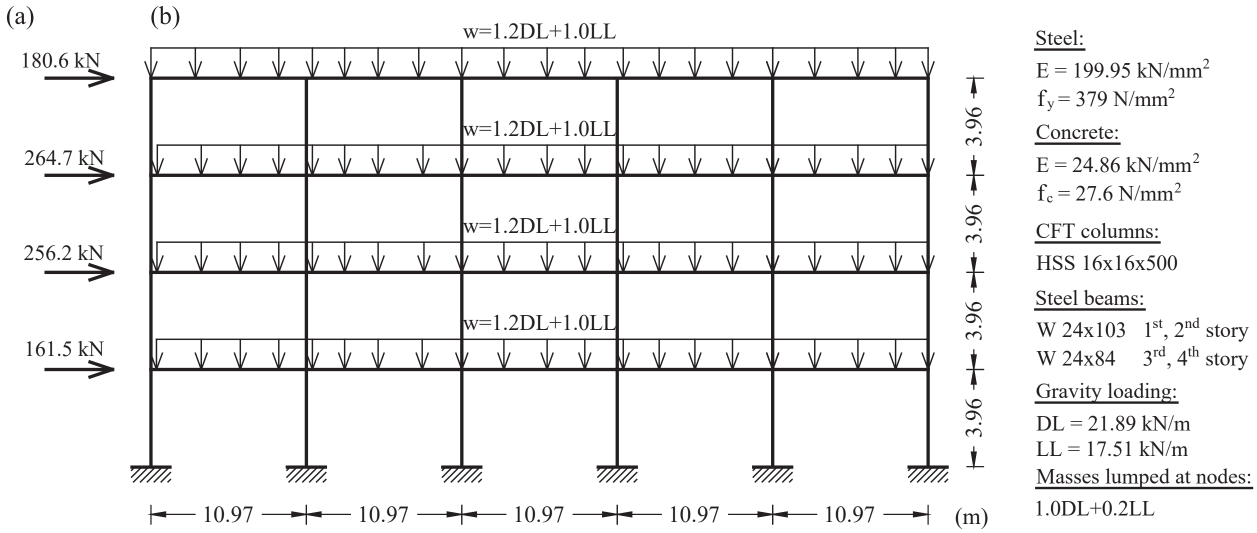

Fig. 20. Composite plane moment frame: (a) Distribution of lateral forces in the pushover analysis; (b) Geometric, material and loading information

damping ratio of 2.5% for the first mode.

The model of the composite frame uses a single fiber beam-column element for each column and girder. The element uses the force formulation with 4 Gauss-Lobatto integration points for the columns, and 5 Gauss-Lobatto integration points for the girders. The control sections of the girders use 2 fibers in each flange and 8 fibers in the web for the determination of the stiffness and the resisting forces under uniaxial bending. Instead, the columns use a 3d fiber section discretization regardless of the fact that the response is also uniaxial. The reference discretization of the column sections for the "numerically exact" response uses 10 fibers on each side of the steel tube with a single fiber across the thickness and a 10x10 fiber mesh for the concrete core. At the start of the analysis the section response is determined with the scheme in Fig. 6(c), while the final section discretization after activation of all tubular "rings" is shown in Fig. 6(d). The GMP model is used for the steel tube material with yield strength f_y = 379 MPa, initial modulus E_s = 199.95 GPa, and kinematic strain hardening ratio of 1.5%. The Mander model is used for the concrete with the compressive strength equal to f_c' = 27.6MPa and the modulus of elasticity E_c = 24860 MPa. For the concrete confined by the steel tube a strength increase factor of $K = 1.25$ is used in the model. The ring activation criterion is based again on the trigger strain limits $e_{lim,2}$ or $e_{lim,3}$.

Fig. 21(a) shows the roof drift ratio history and Fig. 21(b) shows the relation between roof drift ratio and base shear for the dynamic response of the composite frame under the ground acceleration for the LA23 record. The adaptive section discretization with either ring activation criterion matches the reference response extremely well in Fig. 21. The adaptive section discretization with trigger strain limits $e_{lim,2}$ reduces the computation time by 38% relative to the reference solution, while the alternative criterion with trigger strain limits $e_{lim,3}$ reduces the computation time by 58%. A further reduction of the computation time is possible with the use of the adaptive section discretization for the wide flange beam sections which number 100 in the structural model, but the subject is left for future studies.

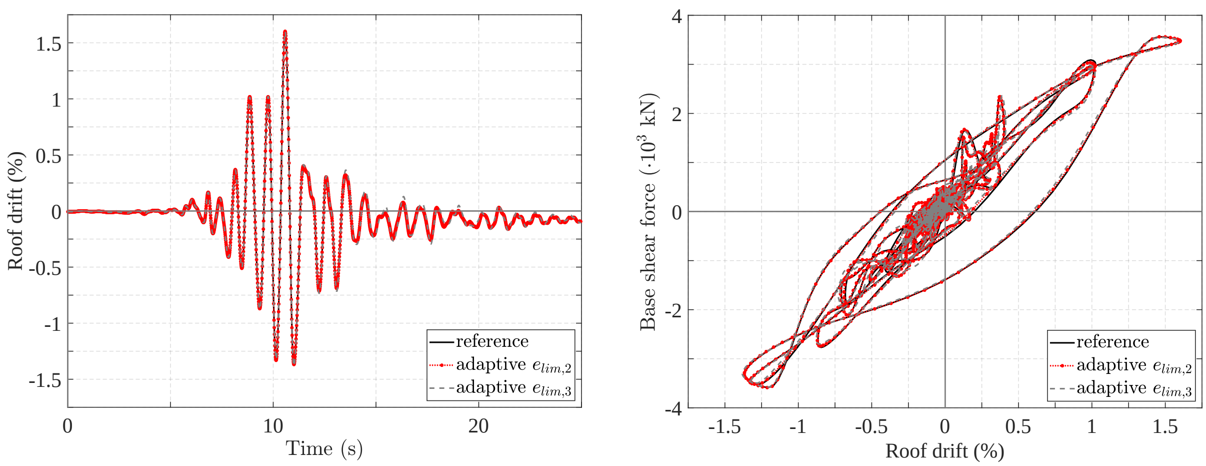

(a) Roof drift history in X direction

(b) Roof drift ratio vs. base shear force

Fig. 21. Composite frame response under the ground acceleration for the LA23 record

Fig. 22 shows the relation between the roof story drift ratio and the base shear for the nonlinear pushover analysis of the composite frame. The adaptive section discretization with either ring activation criterion matches again the reference response extremely well. The markers for the activation of the first and the last section under the two activation criteria show the very early activation of the first section under the trigger strain limits $e_{lim,2}$, because of the early appearance of tensile cracking in the concrete core of the columns. Consequently, almost 95% of the column sections are active at the end of the analysis. In contrast, the activation of the first section for the trigger strain limits $e_{lim,3}$ takes place much later, with only 22% of the column sections having at least one tubular "ring" activated at the end of the analysis. The resulting savings in computation time are similar to those for the dynamic analysis with the adaptive solution for the trigger strain limits $e_{lim,2}$ 60% faster than the reference solution, while the adaptive solution with trigger strain limits $e_{lim,3}$ reduces the computation time by 75%, as summarized in Table 2.

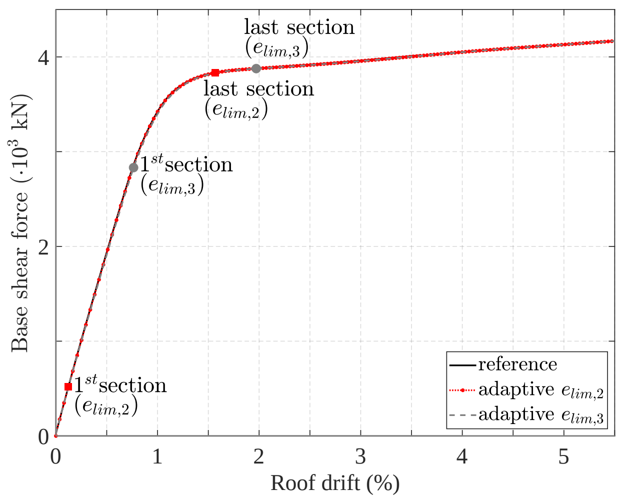

Fig. 22. Pushover response of composite frame with markers for first and last section activation

TABLE 2. Calculation times of 2d composite frame analysis

Analysis	Reference	Adaptive $e_{lim,2}$	Adaptive $e_{lim,3}$
Dynamic	100%	62%	42%
Pushover	100%	40%	25%

CONCLUSIONS

The paper presents an adaptive section discretization scheme for the inelastic response of moment-resisting frames with fiber beam-column elements. The scheme is based on the use of cubature rules for the exact evaluation of the section response before the onset of nonlinear material response. Once the strain exceeds specific trigger values, the section discretization uses a mesh with midpoint integration over the nonlinear portion of the section and the cubature rule over the linear portion. Because the adaptive discretization takes place at the section level, the proposed scheme can be used with any beam-column element that bases the section response on the numerical integration of the material stress-strain relation over the section.

The examples in the paper for 2d and 3d frames with members having rectangular or circular cross-sections of any material demonstrate that the proposed adaptive discretization gives results of remarkable accuracy while resulting in computational savings from 30% to 75% relative to the reference solution with an a-priori section mesh discretization. The time savings depend on the target strain activation criterion. Strict target strain limits result in many more ring activations during the analysis and smaller computational time savings. The inelastic response studies show that even relaxed target strain activation criteria give results of satisfactory accuracy with significant time savings in computation time. The scheme is especially practical by allowing the analyst to customize the target strain activation criteria on the basis of the global and local response accuracy requirements. By varying the target strain activation criteria over the structural model components significant savings of computation time are possible without compromising the response accuracy.

DATA AVAILABILITY STATEMENT

Some or all data, models, or code that support the findings of this study are available from the corresponding author upon reasonable request.

ACKNOWLEDGMENTS

The first author thanks Ministry of Science of the Republic of Serbia for financial support under the project number 2000092.

REFERENCES

Abramowitz, M., Stegun, I. A., and Miller, D. (1965). *Handbook of mathematical functions with formulas, graphs and mathematical tables (National Bureau of Standards Applied Mathematics Series No. 55)*. Cambridge University Press.

Berry, M. P. and Eberhard, M. O. (2008). "Performance modeling strategies for modern reinforced concrete bridge columns." *Report no.*, PEER Report 2007/07, Department of Civil and Environmental Engineering, University of California, Berkeley, CA.

Cohen, J., Filippou, F. C., and Kostic, S. M. (2022). "Discretization schemes for the analysis of circular rc columns under cyclic loading." *Report No. to be published*, PEER Report, Department of Civil and Environmental Engineering, University of California, Berkeley, CA.

Cools, R. (2003). "An encyclopaedia of cubature formulas." *Journal of Complexity*, 19(3), 445–453.

Filippou, F. C. and Constantinides, M. (2004). "Fedeaslab getting started guide and simulation examples." *Technical Report NEESgrid-2004-22*, University of California, Berkeley.

Hajjar, J. F., Molodan, A., and Schiller, P. H. (1998). "A distributed plasticity model for cyclic analysis of concrete-filled steel tube beam-columns and composite frames." *Engineering Structures*, 20(4), 398–412.

He, Z., Fu, S., and Ou, J. (2017a). "State transformation procedures for fiber beam-column element in inelastic dynamic time history analysis for moment-resisting frames." *Journal of Computing in Civil Engineering*, 31(5), 04017036.

He, Z., Fu, S., Shi, Y., Tao, Q., and Sun, C. (2017b). "New speedup algorithms for nonlinear dynamic time history analysis of supertall building structures under strong earthquakes." *The Structural Design of Tall and Special Buildings*, 26(16), e1369.

Hu, J. W. (2008). "Seismic performance evaluations and analyses for composite moment frames with smart sma pr-cft connections." Ph.D. thesis, School of Civil and Environmental Engineering, Georgia Institute of Technology, Atlanta, GA.

(ICC), I. C. C. (2003). *International Building Code (IBC 2003)*. Falls Church, VA.

Izzuddin, B. and Lloyd Smith, D. (2000). "Efficient nonlinear analysis of elasto-plastic 3d r/c frames using adaptive techniques." *Computers and Structures*, 78(4), 549–573.

Kostic, S. and Filippou, F. (2012). "Section discretization of fiber beam-column elements for cyclic inelastic response." *Journal of Structural Engineering*, 138(5), 592–601.

Kostic, S. M. and Deretic-Stojanovic, B. (2016). "Fiber element formulation for inelastic frame analysis." *Građevinski materijali i konstrukcije*, 59(2), 3–13.

Mander, J. B., Priestley, M. J. N., and Park, R. (1998). "Theoretical stress-strain model for confined concrete." *Journal of Structural Engineering ASCE*, 114(8), 1804–1826.

Neuenhofer, A. and Filippou, F. C. (1997). "Evaluation of nonlinear frame finite-element models." *Journal of Structural Engineering*, 123(7), 958–966.

of Steel Construction (AISC), A. I. (2005). *Seismic Provisions for Structural Steel Buildings (ANSI/AISC 341-05)*. Chicago, IL.

Scott, M. H. and Fenves, G. L. (2006). "Plastic hinge integration methods for force-based beam-column elements." *Journal of Structural Engineering*, 132(2), 244–252.

Song, L., Izzuddin, B., Elnashai, A., and Dowling, P. (2000). "An integrated adaptive environment for fire and explosion analysis of steel frames — part i:: analytical models." *Journal of Constructional Steel Research*, 53(1), 63–85.

Tao, M.-X. and Nie, J.-G. (2015). "Element mesh, section discretization and material hysteretic laws for fiber beam–column elements of composite structural members." *Materials and Structures*, 48(8), 2521–2544.

Terzic, V. and Stojadinovic, B. (2015). "Evaluation of post-earthquake axial load capacity of circular bridge columns." *ACI Structural Journal*, 112(1), 23–33.

Zupan, D. and Saje, M. (2005). "Analytical integration of stress field and tangent material moduli over concrete cross-sections." *Computers and Structures*, 83(28), 2368–2380.